Coherent optical control of polarization with a critical metasurface

Kang, Ming; Chong, Yi Dong

2015

Kang, M., & Chong, Y. D. (2015). Coherent optical control of polarization with a critical metasurface. Physical Review A, 92(4), 043826-.

https://hdl.handle.net/10356/81116

https://doi.org/10.1103/PhysRevA.92.043826

Coherent optical control of polarization with a critical metasurface

Ming Kang[1,*] and Y. D. Chong[2,†]
[1]*College of Physics and Materials Science, Tianjin Normal University, Tianjin 300387, China*
[2]*School of Physical and Mathematical Sciences and Centre for Disruptive Photonic Technologies, Nanyang Technological University, Singapore 637371, Singapore*
(Received 28 April 2015; published 19 October 2015)

We present a mechanism by which a metamaterial surface, or metasurface, can act as an ideal phase-controlled rotatable linear polarizer. Using coupled-mode theory and the idea of coherent perfect absorption into auxiliary polarization channels, we show how the losses and near-field couplings on the metasurface can be balanced so that, with equal-power linearly polarized beams incident on each side, varying the relative phase rotates the polarization angles of the output beams while maintaining zero ellipticity. The system can be described by a non-Hermitian effective Hamiltonian which is parity-time (PT) symmetric, although there is no actual gain present; perfect polarization conversion occurs at the eigenfrequencies of this Hamiltonian, and the polarization rotating behavior occurs at the critical point of its PT-breaking transition.

DOI: 10.1103/PhysRevA.92.043826 PACS number(s): 42.25.Bs, 42.25.Ja, 78.67.Pt

I. INTRODUCTION

In photonics, optical loss is commonly regarded as an unwanted nuisance. However, some recent advances have shown that loss can be an interesting control parameter in its own right. A case in point is the phenomenon of coherent perfect absorption (CPA): when the loss in an optical structure is tuned to an appropriate (noninfinite) level, a specific incident wavefront is absorbed without scattering [1–11]. This is a generalization of the phenomenon of "critical coupling" [1], and in a multichannel system, like a metamaterial surface, or "metasurface" [12], with waves incident from both sides, it provides a way to control light with light without optical nonlinearity [5–7]: varying part of the incident wavefront, such as the phase of one input beam, can switch the whole wavefront between perfect and near-zero absorption. Another example of loss as a control parameter comes from the field of parity-time (PT) symmetric optics, which deals with structures containing spatially balanced gain and loss [13–27]. Such devices exhibit a form of non-Hermitian symmetry breaking [13], whose "critical point" or "exceptional point" [15] can produce extraordinary behaviors such as unidirectional invisibility [16–19,24–27]. Intriguingly, several links have been found between PT symmetry and CPA: PT-symmetric scatterers can simultaneously exhibit CPA and lasing [20,22,23], and in some metasurfaces the occurrence of CPA can be mapped to the PT-breaking transition of an effective Hamiltonian [28].

The theory of CPA is agnostic about the nature of the loss [1], which can be some combination of Ohmic loss, fluorescence, or radiation into other coherent channels [29,30]. At first glance, treating radiative loss using the language of CPA may seem pointless, for the "absorption" of light from one input channel into another channel occurs in so simple a system as a nonscattering waveguide. However, when *multiple* scattering channels are present, it provides an interesting way to control optical polarization [31–33].

Several groups have recently implemented polarization-manipulating metasurfaces [34–37] based on the idea of varying structural elements at different spatial positions in order to generate anomalous phase responses in the reflected and/or transmitted beams. Since the polarization state is determined by the structural features of the metasurface, however, achieving dynamic control is a challenging task.

One promising alternative approach was explored in recent experiments by Mousavi *et al.* [32,33]. They showed that when two equal-power linearly polarized beams are incident on a chiral metasurface, varying the relative phase ϕ between the beams can induce a complete rotation of each output beam's polarization angle, with ellipticity $\lesssim 15^\circ$. The metasurface thus acts as a polarization rotator controlled by ϕ. However, the underlying physical mechanism has not yet been analyzed in detail. Mousavi *et al.* noted that, for one input beam, the transmission is approximately circularly polarized, say, left-circularly polarized (LCP). To rotate the polarization, the reflection of the input beam incident from the opposite side must be right-circularly polarized (RCP). This implies, by mirror symmetry along the beam axis, that for each input beam the reflection and transmission have the *same* handedness, which is counterintuitive since a mirror-symmetric chiral resonance emits to each side with *opposite* handedness. As we shall see, this simple explanation is incomplete. A metasurface can generate rotatable output beams with exactly zero ellipticity but only when tuned to a certain CPA-like condition, and the polarization under single-sided illumination is typically elliptical rather than circular.

Here, we present a theoretical study of an ideal two-sided polarization-rotating metasurface, which reveals deep ties to the concepts of CPA [1–11] and PT symmetry [13–28]. The metasurface contains pairs of resonators radiating into different linear polarization channels, subject to dissipation and near-field coupling. Using coupled-mode theory (CMT) [38–44], we show that it can perform "perfect polarization conversion" (PPC) of two linearly polarized input beams (i.e., 90° rotation with zero ellipticity). PPC requires a specific balance between the radiative loss rates, dissipation rates, and near-field coupling rates of the metasurface resonators. This is analogous to ordinary CPA, which occurs at discrete loss

*mingkang@mail.nankai.edu.cn
†yidong@ntu.edu.sg

levels [1]. The coupled-mode analysis also shows that the frequencies for PPC are eigenvalues of an effective Hamiltonian which is PT symmetric, although the metasurface itself is gain free. (Similar mappings to PT-symmetric Hamiltonians have been explored for CPA [28] and for polarization conversion under one-sided transmission [45].) For "critical" solutions to the PPC conditions, corresponding to PT transition points of the effective Hamiltonian, the metasurface acts as an ideal polarization rotator: as we vary the relative input phase ϕ, the output beams remain linearly polarized, and their polarization angles undergo complete rotations. The efficiency approaches 100% when the radiative loss and coupling rates dominate the dissipation. Under one-sided illumination, the reflected and transmitted beams have equal handedness due to interference between direct and indirect transmissions, but the critical metasurface is generally *not* a perfect circular polarizer under one-sided illumination; the above-mentioned explanation involving RCP and LCP components [32,33] holds only for zero dissipation. For nonzero dissipation, the reflection and transmission on each side are elliptically polarized but can nonetheless combine to ensure zero total ellipticity. With other parameters choices, we can also switch the outputs between circular and linear polarization by varying ϕ. Full-wave simulation results verify the predictions of the CMT.

II. THEORETICAL MODEL

Consider the plane metasurface depicted in Fig. 1(a). It is mirror symmetric along the normal $\hat{z}$ and contains pairs of modes described by complex amplitudes $\vec{q} \equiv [q_x, q_y]^T$, radiating in the $\hat{x}$ and $\hat{y}$ linear polarizations, respectively. Plane waves are normally incident on each side, with amplitudes $\vec{a} = [a_{h+}, a_{h-}, a_{v+}, a_{v-}]^T$, where $+$ $(-)$ denotes incidence from the top (bottom) and $h(v)$ denotes linear polarization parallel to $\hat{x}(\hat{y})$. The outputs are described by $\vec{b} = [b_{h+}, b_{h-}, b_{v+}, b_{v-}]^T$, with $\pm$ denoting waves exiting to $\pm\hat{z}$. This system can be described by coupled-mode equations [38–44]:

$$-i\,\boldsymbol{\Omega}\,\vec{q} = \mathbf{K}\,\vec{a}, \tag{1a}$$

$$\mathbf{K}^T\,\vec{q} + \mathbf{C}\,\vec{a} = \vec{b}, \tag{1b}$$

where

$$\boldsymbol{\Omega} = \begin{pmatrix} \delta_x - i\left(\gamma_x^s + \gamma_x^d\right) & -\kappa \\ -\kappa & \delta_y - i\left(\gamma_y^s + \gamma_y^d\right) \end{pmatrix}, \tag{2a}$$

$$\mathbf{K} = \begin{pmatrix} \sqrt{\gamma_x^s} & \sqrt{\gamma_x^s} & 0 & 0 \\ 0 & 0 & \sqrt{\gamma_y^s} & \sqrt{\gamma_y^s} \end{pmatrix}, \tag{2b}$$

$$\mathbf{C} = \begin{pmatrix} \sigma_1 & \mathbf{0} \\ \mathbf{0} & \sigma_1 \end{pmatrix}, \quad \sigma_1 \equiv \begin{pmatrix} 0 & 1 \\ 1 & 0 \end{pmatrix}. \tag{2c}$$

Here, δ_μ (where $\mu \in \{x, y\}$) is the frequency detuning from the μ-oriented resonance, γ_μ^s is the radiative scattering rate, γ_μ^d is the dissipation rate, and κ is the near-field coupling between the modes; all these parameters are real. $\mathbf{K}$ is the radiative coupling between the metasurface and the input and output waves, while $\mathbf{C}$ is the direct coupling. These matrices are constrained by the mirror symmetry, the definitions of energy and power, and optical reciprocity [39]. The scattering matrix

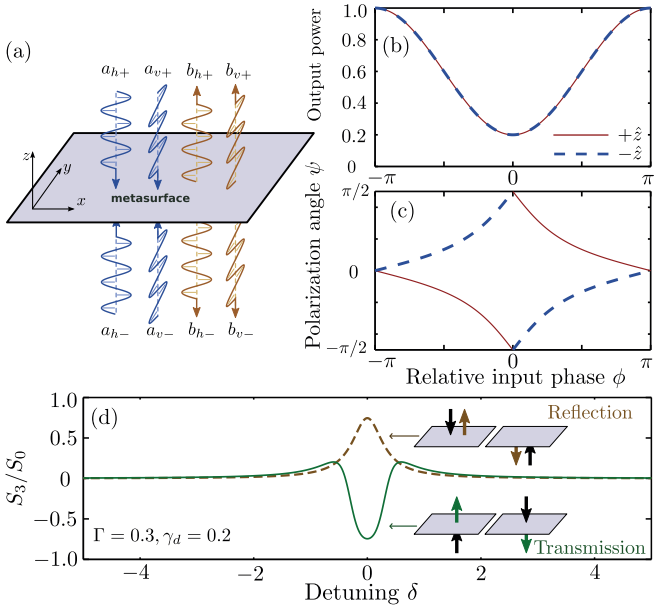

FIG. 1. (Color online) (a) Schematic of the input and output wave amplitudes $\vec{a}$ and $\vec{b}$. (b) Output power $S_0 = |b_{h+}|^2 + |b_{h-}|^2$ vs relative phase $\phi \equiv \arg(a_{h-}/a_{h+})$ of the input beams. The critical metasurface parameters are $\kappa = \Gamma = 0.3$ and $\gamma_d = 0.2$. Each input beam has unit power. The efficiency depends on the choice of γ_d/Γ; here, ∼80% is absorbed at $\phi = 0$ for $\gamma_d/\Gamma = 0.667$, whereas in Fig. 4, ∼20% is absorbed for $\gamma_d/\Gamma = 0.07$. (c) Polarization angle $\psi = \tan^{-1}(S_2/S_1)/2$. The outputs are linearly polarized ($S_3 = 0$) for all ϕ. (d) Ellipticity parameter S_3/S_0 vs detuning δ of a single input beam, transmitted from $\pm\hat{z}$ to $\mp\hat{z}$ (solid curve) and reflected from $\pm\hat{z}$ to $\pm\hat{z}$ (dashed lines). Note that neither beam is circularly polarized at $\delta = 0$.

$\mathbf{S}$, defined by $\mathbf{S}\,\vec{a} = \vec{b}$, is

$$\mathbf{S} = \mathbf{C} + i\,\mathbf{K}^T\boldsymbol{\Omega}^{-1}\mathbf{K} \equiv \begin{pmatrix} \mathbf{S}_x & \mathbf{D} \\ \mathbf{D} & \mathbf{S}_y \end{pmatrix}. \tag{3}$$

$\mathbf{S}_x$ ($\mathbf{S}_y$) describes how light incident in the $h(v)$ polarization scatters into the same polarization, while $\mathbf{D}$ describes the cross-polarized scattering.

We now assume that the metasurface is designed so the resonances have the same dissipation rates and frequencies:

$$\gamma_x^d = \gamma_y^d \equiv \gamma_d, \quad \delta_x = \delta_y \equiv \delta. \tag{4}$$

(The radiative scattering rates, however, can and will differ.) Furthermore, we consider h-polarized incident illumination, with amplitudes $\vec{a}_h = [a_{h+}, a_{h-}]^T$, so the outputs are $\vec{b}_h = \mathbf{S}_x\,\vec{a}_h$ and $\vec{b}_v = \mathbf{D}\,\vec{a}_h$. Due to the mirror symmetry, $\mathbf{S}_x$ has eigenvectors $[1,1]^T$ and $[1,-1]^T$; the latter, with eigenvalue -1, corresponds to a node on the plane experiencing zero total loss.

By varying the metasurface parameters and input amplitudes, we can arrive at a situation where $\vec{b}_h = 0$, i.e., all the h-polarized incident light is reemitted in the v polarization and/or dissipated. We call this perfect polarization conversion. It corresponds to CPA with v-polarized emission as an "absorption" channels (it would be ordinary CPA if $\gamma_y^s = 0$).

For PPC to occur, the symmetric eigenvector of $\mathbf{S}_x$ must have eigenvalue zero; this occurs if and only if

$$\gamma_x^s - \gamma_d = \gamma_y^s + \gamma_d \equiv \Gamma, \tag{5a}$$

$$\delta^2 = \kappa^2 - \Gamma^2. \tag{5b}$$

If $|\kappa| > \Gamma$, Eq. (5b) can be satisfied at two distinct frequencies. But if $|\kappa| < \Gamma$, it cannot be satisfied for any δ.

We can interpret Eqs. (5a)–(5b) in terms of an effective Hamiltonian [28]. Starting from Eq. (3), we can write $\det(\mathbf{S}_x) = \det(\mathbf{H}_x - \delta \cdot \mathbf{I})/[-\det(\mathbf{\Omega})]$, where

$$\mathbf{H}_x = \begin{pmatrix} i(\gamma_d - \gamma_x^s) & \kappa \\ \kappa & i(\gamma_d + \gamma_y^s) \end{pmatrix}. \tag{6}$$

The eigenvalues of $\mathbf{H}_x$ are detunings for which PPC occurs. These should be real, but $\mathbf{H}_x$ is non-Hermitian. However, $\mathbf{H}_x$ becomes PT symmetric [13], with $\mathbf{P} = \sigma_1$ and $\mathbf{T}$ being the complex conjugation operation, when Eq. (5a) is satisfied. Then the eigenvalues become $\pm\sqrt{\kappa^2 - \Gamma^2}$, which are the solutions to Eq. (5b) and are real for the PT-unbroken phase of $\mathbf{H}_x$, $|\kappa| > \Gamma$. In the PT-broken phase, $|\kappa| < \Gamma$, PPC cannot occur for any real δ. At $\kappa = \pm\Gamma$, which are the critical points of Eq. (5b) and the PT transition points [15] of $\mathbf{H}_x$, PPC occurs only at $\delta = 0$. As in Ref. [28], we can also think of the metasurface as a platform for realizing PT-symmetric Hamiltonians.

Now suppose the metasurface is tuned to one of the critical points, satisfying Eqs. (5a)–(5b) with $\kappa = \Gamma$, $\delta = 0$. For h-polarized inputs, the coupled-mode equations give

$$b_{h\pm} = \mp\frac{1}{2}(a_{h+} - a_{h-}), \tag{7}$$

$$b_{v\pm} = -\frac{i}{2}\sqrt{\frac{\Gamma - \gamma_d}{\Gamma + \gamma_d}}(a_{h+} + a_{h-}). \tag{8}$$

The outputs have equal power and third Stokes parameters

$$S_3^{\pm} \equiv -2\mathrm{Im}[b_{h\pm}b_{v\pm}^*] = \pm\sqrt{\frac{\Gamma - \gamma_d}{\Gamma + \gamma_d}}\,\frac{|a_{h+}|^2 - |a_{h-}|^2}{2}. \tag{9}$$

Hence, for equal-power inputs ($|a_{h+}|^2 = |a_{h-}|^2$), both outputs are exactly linearly polarized ($S_3^{\pm} = 0$).

Part of this result is easy to understand: the outputs are v polarized for symmetric inputs (PPC) and h polarized for antisymmetric inputs (node on the plane). But Eq. (9) goes further and states that the output beams are linearly polarized for *all* input beam phases. Varying the relative phase rotates the output beams' polarization angles between $[0,\pi/2]$. This behavior is specific to the critical metasurface. (At the other critical point, $\kappa = -\Gamma$, the polarization rotates in the opposite direction; $\kappa \neq 0$ implies broken left-right symmetry.)

The action of the critical metasurface as a rotatable linear polarizer is shown in Figs. 1(b) and 1(c). The efficiency is characterized by the ratio of total output to input power at $\phi = \arg(a_{h-}/a_{h+}) = 0$ (peak dissipation, coinciding with PPC). This ratio is $(\Gamma - \gamma_d)/(\Gamma + \gamma_d)$, so for $\gamma_d \ll \Gamma$ the loss is $\approx 4\gamma_d/\Gamma$, and the polarization angle is $\psi \approx (\pi \pm \phi)/2$ for the $\pm\hat{z}$ outputs. Here, the efficiency is low because we have chosen relatively large $\gamma_d/\Gamma = 0.667$ to clarify the relative contributions of dissipation and radiative scattering; we will shortly consider a more efficient case. (For $\Gamma/\gamma_d = 1$, the $\hat{y}$ resonance is dark, and the system reduces to the CPA metasurface of Ref. [28].)

Consider the reflection and transmission of a one-sided h-polarized input beam at the critical point. As shown in Fig. 1(d), $S_3 > 0$ for reflection and $S_3 < 0$ for transmission for either choice of input direction; that is, reflection and transmission have the same handedness. The coupled-mode analysis clarifies why this happens: the transmitted beam consists of both direct transmission and chiral reemission from the resonances. At the critical point, the total transmitted beam has handedness opposite to its reemitted component and the same as the reflected beam. The transmission and reflection are *not* circularly polarized, except when $\gamma_d \to 0$. Under two-sided illumination, the elliptical beam components combine to form linearly polarized output beams.

Away from the critical point, the metasurface ceases to act as a linear polarizer, but a remnant of the critical behavior persists. At the critical point, one cycle of ϕ winds each output amplitude along the equator of the Poincaré sphere, as shown in Figs. 2(a) and 2(b). Away from the critical point, the trajectory no longer follows the equator exactly, but one cycle of ϕ still induces one winding of $2\psi \equiv \tan^{-1}(S_2/S_1)$ and hence a full cycle of the polarization ellipse's semimajor axis. This holds as long as the loops do not cross the poles, which occurs at

$$\delta^2 = \kappa^2 - \Gamma^2 \pm 2\kappa\sqrt{\Gamma^2 - \gamma_d^2}. \tag{10}$$

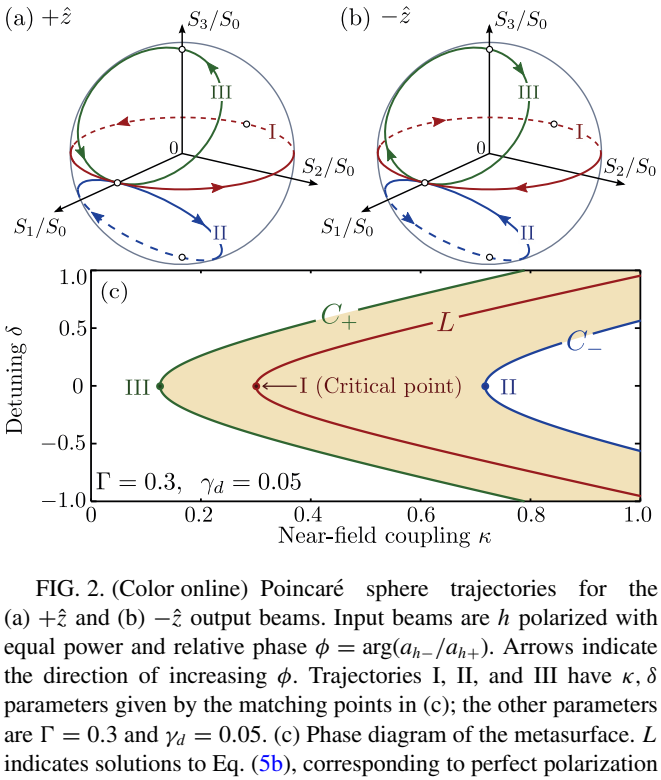

FIG. 2. (Color online) Poincaré sphere trajectories for the (a) $+\hat{z}$ and (b) $-\hat{z}$ output beams. Input beams are h polarized with equal power and relative phase $\phi = \arg(a_{h-}/a_{h+})$. Arrows indicate the direction of increasing ϕ. Trajectories I, II, and III have κ, δ parameters given by the matching points in (c); the other parameters are $\Gamma = 0.3$ and $\gamma_d = 0.05$. (c) Phase diagram of the metasurface. L indicates solutions to Eq. (5b), corresponding to perfect polarization conversion, i.e., real eigenvalues of the PT-symmetric matrix (6). $C_\pm$ indicate solutions of Eq. (10), for which the output are circularly polarized. The $\kappa < 0$ region, not shown here, has a similar form.

For $\kappa > 0$, the $+$ $(-)$ sign corresponds to an RCP (LCP) $+\hat{z}$ output and an LCP (RCP) $-\hat{z}$ output. Hence, we obtain the "phase diagram" shown in Fig. 2(c). The curves $C_\pm$ indicate solutions to Eq. (10), where varying ϕ switches the output between linear and circular polarizations, as shown in Figs. 2(a) and 2(b). In the region between these curves, 2ψ undergoes a complete winding with ϕ. The phase diagram for $\kappa < 0$ is similar.

III. NUMERICAL RESULTS

The CMT is quite general, given the assumptions that (i) the metasurface resonances can be decomposed into a pair of q_x and q_y components, (ii) the system is mirror symmetric along the $\hat{z}$ axis, and (iii) the scattering in the absence of the resonances can be described by Eq. (2c). To verify it, we design an exemplary plasmonic metasurface, shown in Fig. 3(c). Each unit cell contains a silver strip antenna radiating in the $\hat{x}$ direction and a silver split-ring resonator (SRR) radiating in $\hat{y}$. The cells are arranged in a square lattice with period $d = 600$ nm, and the entire metasurface is freestanding in vacuum. No high-order diffraction mode exists below 500 THz. The dielectric function of silver is modeled by a Drude formula $\varepsilon_m = \varepsilon_\infty - f_p^2/(f^2 + i\gamma_p f)$, where $f_p = 2230$ THz, $\gamma_p = 5.09$ THz, and $\varepsilon_\infty = 5$. To extract the coupled-mode parameters for each resonator, we perform full-wave (finite-difference time-domain) numerical simulations with single-sided incident illumination in the absence of the other resonator, with the appropriate linear

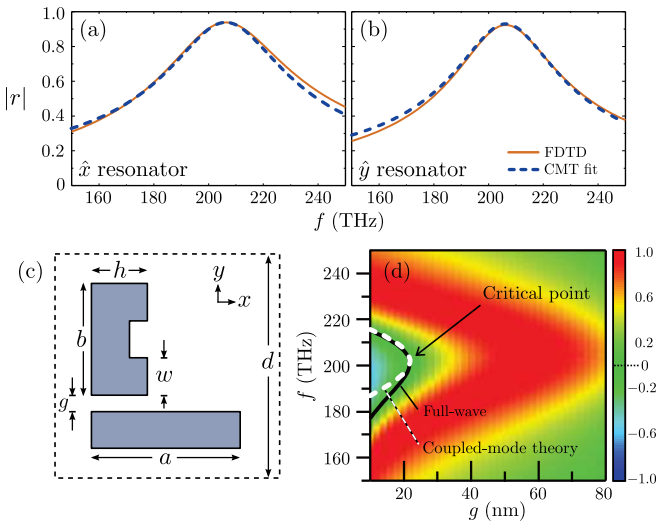

FIG. 3. (Color online) Design of the critical metasurface. (a) Reflectance of a strip antenna with $a = 434.25$ nm and $w = 50$ nm. (b) Reflectance of a split-ring resonator (SRR) with $w = 50$ nm, $b = 355$ nm, $h = 105$ nm. Both antennas are freestanding, with thickness $t = 30$ nm and lattice period $d = 600$ nm; incident light is linearly polarized parallel to their main axes. Solid lines show full-wave simulation results, and dashed lines show least-squares fits to coupled-mode predictions. (c) Schematic of the unit cell. (d) Full-wave results for S_3/S_0 vs resonator separation g and operating frequency f for the $+\hat{z}$ output beam with symmetric equal-power inputs. The dashed line show where Eq. (5b) is satisfied using fitted coupled-mode parameters; the solid line shows where $S_3 = 0$ in the simulation results.

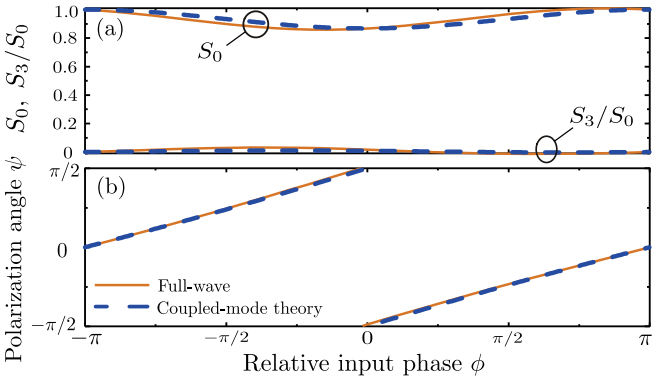

FIG. 4. (Color online) Intensity S_0, ellipticity parameter S_3/S_0, and polarization angle ψ for the $+\hat{z}$ output beam vs the relative phase ϕ of the input beams. The metasurface is at the critical point indicated in Fig. 3(d). Solid curves show full-wave simulation results, and dashed curves show coupled-mode predictions using best-fit parameters.

polarization. The reflectance spectrum is fitted to the theoretical curve $R = \gamma_\mu^{s\,2}/[(f - f_\mu)^2 + (\gamma_\mu^s - \gamma_\mu^d)^2]$ obtained from Eqs. (1b)–(2c) for $\kappa = 0$. Using the structure parameters stated in Fig. 3, each resonator has $f_x = f_y = 206.3$ THz and $\gamma_x^d = \gamma_y^d = 1.3$, satisfying Eq. (4). The radiative decay rates are $\gamma_x^s = 19.8$ THz and $\gamma_y^s = 17.2$ THz, satisfying Eq. (5a).

We now include both resonators, separated by distance g. Varying g, with all other structural parameters fixed, alters the near-field coupling κ, as well as (weakly) the resonant frequency f_0 (see Appendix A). A nonlinear least-squares fit yields $\kappa \approx (28.32 - 0.51g + 0.0026g^2)$ THz and $f_0 \approx (200.48 + 0.073g)$ THz, with g in units of nanometers. The fitted CMT agrees well with simulation results for all output Stokes parameters. For instance, Fig. 3(d) shows S_3/S_0. The locus of $S_3 = 0$ according to the simulation (black line) closely matches the coupled-mode prediction (white dashed line). Based on Eq. (5b), the critical point occurs at $g \approx 22$ nm, $f \approx 202$ THz. Figure 4 shows the critical behavior, which agrees well with the CMT, particularly with the fact that $S_3 \approx 0$ for all ϕ. The peak absorption is less than 20% and could be further reduced by designing antennas with larger radiative decay rates relative to γ_d.

We have focused on a simple metasurface with two antennas per unit cell since that can be easily mapped to the CMT. In particular, the amplitudes $q_{x,y}$ are excitations of the individual antennas. However, the CMT can also be applied to more complicated metasurfaces, such as those in previous experiments [32,33]. In such cases, $q_{x,y}$ would be the decompositions of some spatially complex resonances into eigenmodes radiating into exclusive linear polarization channels, so the mapping between the metasurface parameters and the coupled-mode parameters would be more complicated. In Appendix B, we show that a variant of the theory can describe a "complementary" metasurface consisting of air slits on a metal film.

IV. CONCLUSION

We have shown that the principles of CPA and PT symmetry can be used to analyze metasurfaces that can

manipulate optical polarization with two input beams. This is an example of an emerging class of photonic devices which exploit the properties of "critical" or "exceptional" points [24,27,46,47]. Here, the critical behavior gives rise to exactly zero-ellipticity output beams; devices performing other types of polarization control, such as switching between circular and linear polarization, might also be interesting to study.

ACKNOWLEDGMENTS

M.K. acknowledges supports from the National Natural Science Foundation of China under Grant No. 11304226 and the China Postdoctoral Science Foundation under Grant No. 2014M560414. C.Y.D. acknowledges support from the Singapore National Research Foundation under Grant No. NRFF2012-02 and the Singapore MOE Academic Research Fund Tier 3 Grant No. MOE2011-T3-1-005. We are grateful to N. I. Zheludev, R. Singh, C. Altuzarra, and S. Vezzoli for helpful discussions and comments.

APPENDIX A: FITTING CMT PARAMETERS TO NUMERICAL SIMULATIONS

In order to verify the CMT, we perform finite-difference time-domain (FDTD) simulations of the metasurface with a normally incident plane wave on one side, polarized such that the **E** field is parallel to the metallic strip shown in Fig. 3 (i.e., the $\pm\hat{x}$ direction). Figure 5 plots the intensities reflected into each linear polarization channel, $|r_{xx}|^2$ [Fig. 5(a)] and $|r_{yx}|^2$ [Fig. 5(c)], for frequency f ranging from 150 to 250 THz and interresonator distance g ranging from 10 to 80 nm. All other geometry parameters are fixed at the previous values.

We use these results to fit two CMT parameters: the near-field coupling κ and the resonator frequency f_0. The other CMT parameters, Γ and γ_d, are assumed to be the same as for the isolated (noncoupled) resonators, and their values have been extracted using a separate set of FDTD simulations (see Fig. 3). We find it necessary to treat f_0 as a function of g because each resonant antenna in the hybridized metasurface undergoes a slight frequency shift, possibly arising from a small scattering response in the crossed polarization direction. For each value of g, we perform nonlinear least-squares fits for κ and f_0 using the numerical reflection spectra. Next, we use least-squares polynomial fits to obtain the CMT parameters as functions of g. The results are

$$\kappa \approx 28.32 - 0.51g + 0.0026g^2, \tag{A1}$$

$$f_0 \approx 200.48 + 0.073g, \tag{A2}$$

where both κ and f_0 are given in units of terahertz and g is in nanometers. Using these fitted parameters, the CMT results are shown in Figs. 5(b) and 5(d) and agree well with the full-wave simulations. The fitted κ and f_0 parameters are plotted in Figs. 5(e) and 5(f).

Next, we study the intensity and polarization characteristics of the output beams under two-sided illumination, with symmetric and h-polarized input beams. From Eqs. (2a)–(4),

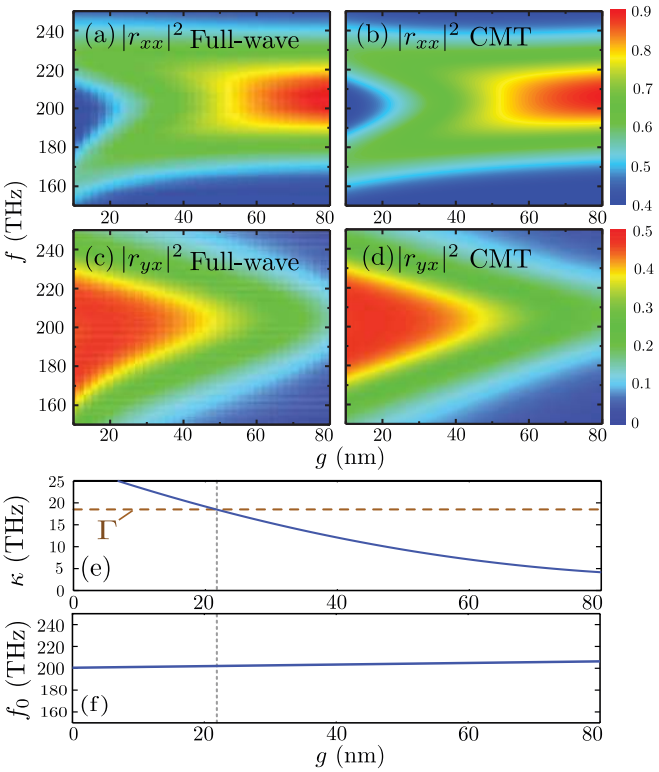

FIG. 5. (Color online) (a) Reflectance into the h channel $|r_{xx}|^2$ for a one-sided h-polarized input beam vs interresonator distance g and frequency f. (b) CMT results using best-fit parameters. (c) Reflectance into the v channel $|r_{yx}|^2$. (d) CMT results for $|r_{yx}|^2$ using the best-fit parameters. (e) and (f) Variation of the CMT parameters κ and f_0 vs g.

the Stokes parameters for the $+\hat{z}$ output beam are

$$S_0 = \frac{1}{|\det \mathbf{\Omega}|^2}\left[(\delta^2+\Gamma^2)^2 + 2\left(\Gamma^2 - \delta^2 - 2\gamma_d^2\right)\kappa^2 + \kappa^4\right], \tag{A3}$$

$$S_1 = \frac{1}{|\det \mathbf{\Omega}|^2}\left[(\delta^2+\Gamma^2)^2 - 2\left(3\Gamma^2 + \delta^2 - 2\gamma_d^2\right)\kappa^2 + \kappa^4\right], \tag{A4}$$

$$S_2 = 0, \tag{A5}$$

$$S_3 = \frac{1}{|\det \mathbf{\Omega}|^2}\, 4\kappa\sqrt{\Gamma^2 - \gamma_d^2}\,(\delta^2 + \Gamma^2 - \kappa^2). \tag{A6}$$

Figure 6 plots the normalized Stokes parameters (S_0, S_1/S_0, S_2/S_0, and S_3/S_0) for the $+\hat{z}$ output beam versus g and f. The full-wave simulation results agree well with the CMT predictions, which are obtained using the same fitted parameters discussed in the previous paragraph. In Fig. 6(g), along the indicated locus of points where $S_3 = 0$, Eq. (5) is satisfied; that is, the incident h-polarized input beams are perfectly converted to the v polarization (as well as partly lost to dissipation). In Figs. 6(e) and 6(f), note that $S_2 = 0$ throughout the investigated parameter range, as predicted in Eq. (A5). Hence, the locus of points indicated in Fig. 6(c), where $S_1 = 0$, corresponds to the C_+ curve as described in

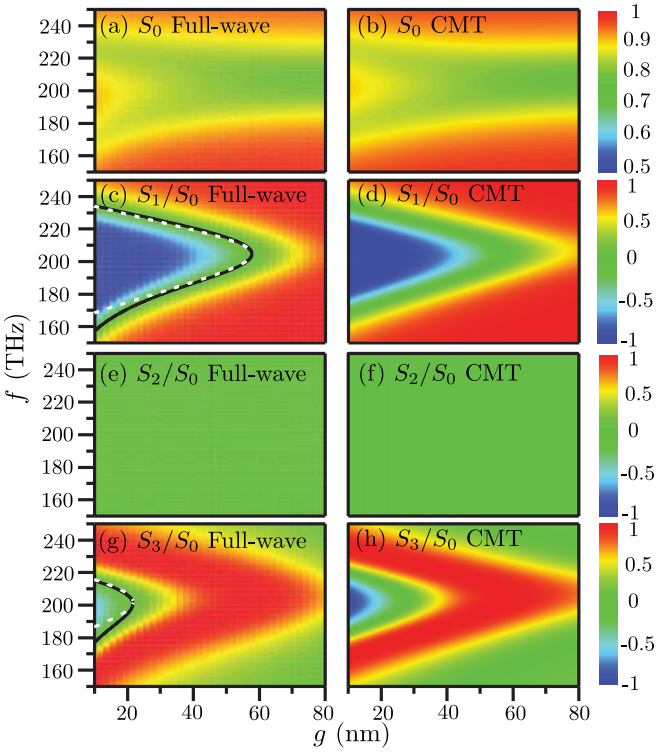

FIG. 6. (Color online) Normalized Stokes parameters for the $+\hat{z}$ output beam vs g and f. In (c) and (g), solid black curves indicate where the Stokes parameter vanishes, and white dashed curves show best-fit CMT predictions.

Eq. (10), where the outputs become circularly polarized for symmetric input beams. (In the investigated metasurface, the other pole crossing does not occur, as κ does not meet the requirements for C_-.)

By tuning the metasurface to the critical point of the C_+ line, we can switch the outputs between circular and linear polarization by varying the relative phase of the inputs ϕ. The determination of this critical point is quite similar to the L critical point. Using the full-wave simulation results, we locate the C_+ critical point at $f = 204.75$ THz, $g = 58$ nm. Figure 7(a) plots the output power of the $+\hat{z}$ output beam versus ϕ. The polarization conversion is relatively efficient, with a maximum of ∼22% dissipation loss at $\phi = 0$, where

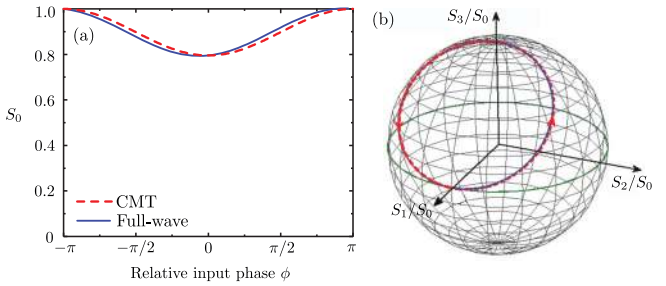

FIG. 7. (Color online) (a) Normalized intensity S_0 of the $+\hat{z}$ output beam at the C_+ critical point vs relative input phase ϕ. FDTD simulation results (red dashes) and best-fit CMT results (blue line) are shown. (b) The Poincaré sphere trajectory touches the C_+ pole as well as the equator.

the output beams become exactly circularly polarized. The Poincaré sphere trajectory of the normalized Stokes parameters as ϕ is varied is shown in Fig. 7(b).

APPENDIX B: NUMERICAL STUDY OF A COMPLEMENTARY METASURFACE

The CMT we have developed is a quite general one and should be applicable to a range of metasurface designs. We demonstrate this by applying it to a structure which is complementary to the one previously discussed. As shown schematically in Fig. 8(g), the structure consists of air holes in a metal surface. The structural parameters are defined in

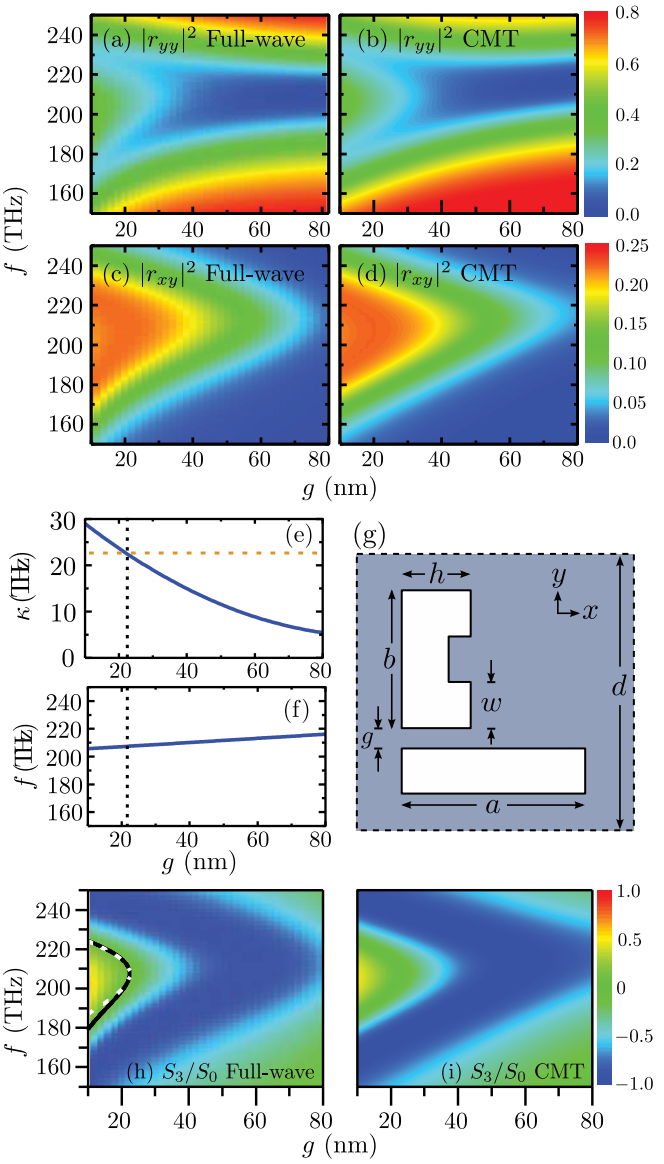

FIG. 8. (Color online) (a)–(d) Reflectance for a one-sided v-polarized input beam, plotted against the interresonator distance g and operating frequency f, using FDTD results and CMT fits. (e) and (f) Variation of the CMT parameters κ and f_0 vs g. (g) Schematic of the air-hole structure. (h) and (i) Normalized S_3 Stokes parameters under two-sided symmetric v-polarized input beams.

the same way as in the original freestanding metasurface structure.

Using the same process to fit the CMT parameters described in Appendix A, we find the dissipation rates are in the form $\gamma_x^d = \gamma_y^d = 1.2$ THz, thus satisfying Eq. (4). Furthermore, the radiative decay rates are $\gamma_x^s = 21.2$ THz and $\gamma_y^s = 23.6$ THz, still satisfying Eq. (5a). For each value of g, the fitted CMT parameters are $\kappa \approx 35.0128 - 0.6336g + 0.0033g^2$ and $f_0 \approx 204.125 + 0.15g$, where both κ and f_0 are also given in units of terahertz and g is in nanometers. Using these fitted parameters, the CMT results are shown in Figs. 8(b) and 8(d) and agree well with the full-wave simulations. The fitted κ and f_0 parameters are also plotted in Figs. 8(e) and 8(f).

Figures 8(h) and 8(i) show the normalized S_3 Stokes parameter for the output under symmetric v-polarized input beams. The full-wave simulation results again agree well with the CMT predictions using fitted parameters. Using Eq. (5b), we find that this structure has a critical point occurring at $g \approx 22.5$ nm, $f \approx 207.5$ THz. We find that $S_2 = 0$ throughout the investigated parameter range, meeting the requirement of Eq. (A5).

[1] Y. D. Chong, L. Ge, H. Cao, and A. D. Stone, Phys. Rev. Lett. **105**, 053901 (2010).
[2] W. Wan, Y. D. Chong, L. Ge, H. Noh, A. D. Stone, and H. Cao, Science **331**, 889 (2011).
[3] S. Longhi, Phys. Rev. A **83**, 055804 (2011).
[4] H. Noh, Y. D. Chong, A. D. Stone, and H. Cao, Phys. Rev. Lett. **108**, 186805 (2012).
[5] J. Zhang, K. F. MacDonald, and N. I. Zheludev, Light Sci. Appl. **1**, e18 (2012).
[6] S. Dutta-Gupta, O. J. Martin, S. D. Gupta, and G. S. Agarwal, Opt. Express **20**, 1330 (2012).
[7] M. Pu, Q. Feng, M. Wang, C. Hu, C. Huang, X. Ma, Z. Zhao, C. Wang, and X. Luo, Opt. Express **20**, 2246 (2012).
[8] N. Gutman, A. A. Sukhorukov, Y. D. Chong, and C. M. de Sterke, Opt. Lett. **38**, 4970 (2013).
[9] M. Kang, F. Liu, T. Li, Q. Guo, J. Li, and J. Chen, Opt. Lett. **38**, 3086 (2013).
[10] M. Kang, Y. D. Chong, H.-T. Wang, W. Zhu, and M. Premaratne, Appl. Phys. Lett. **105**, 131103 (2014).
[11] J. Zhang, C. Guo, K. Liu, Z. Zhu, W. Ye, X. Yuan, and S. Qin, Opt. Express **22**, 12524 (2014).
[12] N. Yu and F. Capasso, Nat. Mater. **13**, 139 (2014).
[13] C. M. Bender and S. Boettcher, Phys. Rev. Lett. **80**, 5243 (1998).
[14] C. M. Bender, M. V. Berry, and A. Mandilara, J. Phys. A **35**, L467 (2002).
[15] S. Klaiman, U. Günther, and N. Moiseyev, Phys. Rev. Lett. **101**, 080402 (2008).
[16] A. Guo, G. J. Salamo, D. Duchesne, R. Morandotti, M. Volatier-Ravat, V. Aimez, G. A. Siviloglou, and D. N. Christodoulides, Phys. Rev. Lett. **103**, 093902 (2009).
[17] C. E. Rüter, K. G. Makris, R. El-Ganainy, D. N. Christodoulides, M. Segev, and D. Kip, Nat. Phys. **6**, 192 (2010).
[18] S. Bittner, B. Dietz, U. Gunther, H. L. Harney, M. Miski-Oglu, A. Richter, and F. Schafer, Phys. Rev. Lett. **108**, 024101 (2012).
[19] A. Mostafazadeh, Phys. Rev. Lett. **102**, 220402 (2009).
[20] S. Longhi, Phys. Rev. Lett. **103**, 123601 (2009).
[21] S. Longhi, Phys. Rev. A **82**, 031801(R) (2010).
[22] Y. D. Chong, L. Ge, and A. D. Stone, Phys. Rev. Lett. **106**, 093902 (2011).
[23] L. Ge, Y. D. Chong, and A. D. Stone, Phys. Rev. A **85**, 023802 (2012).
[24] Z. Lin, H. Ramezani, T. Eichelkraut, T. Kottos, H. Cao, and D. N. Christodoulides, Phys. Rev. Lett. **106**, 213901 (2011).
[25] A. Regensburger, C. Bersch, M.-A. Miri, G. Onishchukov, D. N. Christodoulides, and U. Peschel, Nature (London) **488**, 167 (2012).
[26] G. Castaldi, S. Savoia, V. Galdi, A. Alú, and N. Engheta, Phys. Rev. Lett. **110**, 173901 (2013).
[27] B. Peng, Ş. K. Özdemir, F. Lei, F. Monifi, M. Gianfreda, G. L. Long, S. Fan, F. Nori, C. M. Bender, and L. Yang, Nat. Phys. **10**, 394 (2014).
[28] M. Kang, F. Liu, and J. Li, Phys. Rev. A **87**, 053824 (2013).
[29] M. Crescimanno, N. J. Dawson, and J. H. Andrews, Phys. Rev. A **86**, 031807(R) (2012).
[30] Y. D. Chong, H. Cao, and A. D. Stone, Phys. Rev. A **87**, 013843 (2013).
[31] Y. Wang, M. Pu, C. Hu, Z. Zhao, C. Wang, and X. Luo, Opt. Commun. **319**, 14 (2014).
[32] S. A. Mousavi, E. Plum, J. Shi, and N. I. Zheludev, Appl. Phys. Lett. **105**, 011906 (2014).
[33] S. A. Mousavi, E. Plum, J. Shi, and N. I. Zheludev, Sci. Rep. **5**, 8977 (2015).
[34] N. Yu, F. Aieta, P. Genevet, M. A. Kats, Z. Gaburro, and F. Capasso, Nano Lett. **12**, 6328 (2012).
[35] N. K. Grady, J. E. Heyes, D. R. Chowdhury, Y. Zeng, M. T. Reiten, A. K. Azad, A. J. Taylor, D. A. R. Dalvit, and H.-T. Chen, Science **340**, 1304 (2013).
[36] G. Zheng, H. Mühlenbernd, M. Kenney, G. Li, T. Zentgraf, and S. Zhang, Nat. Nanotechnol. **10**, 308 (2015).
[37] S. C. Jiang, X. Xiong, Y. S. Hu, S. W. Jiang, Y. H. Hu, D. H. Xu, R. W. Peng, and M. Wang, Phys. Rev. B **91**, 125421 (2015).
[38] H. A. Haus, *Waves and Fields in Optoelectronics* (Prentice-Hall, Englewood Cliffs, NJ, 1984).
[39] W. Suh, Z. Wang, and S. Fan, IEEE J. Quantum Electron. **40**, 1511 (2004).
[40] R. E. Hamam, A. Karalis, J. D. Joannopoulos, and M. Soljačić, Phys. Rev. A **75**, 053801 (2007).
[41] S. Zhang, D. A. Genov, Y. Wang, M. Liu, and X. Zhang, Phys. Rev. Lett. **101**, 047401 (2008).
[42] N. Liu, L. Langguth, T. Weiss, J. Kästel, M. Fleischhauer, T. Pfau, and H. Giessen, Nat. Mater. **8**, 758 (2009).
[43] L. Verslegers, Z. Yu, Z. Ruan, P. B. Catrysse, and S. Fan, Phys. Rev. Lett. **108**, 083902 (2012).
[44] P. Tassin, L. Zhang, R. Zhao, A. Jain, T. Koschny, and C. M. Soukoulis, Phys. Rev. Lett. **109**, 187401 (2012).
[45] M. Lawrence, N. Xu, X. Zhang, L. Cong, J. Han, W. Zhang, and S. Zhang, Phys. Rev. Lett. **113**, 093901 (2014).
[46] M. Liertzer, L. Ge, A. Cerjan, A. D. Stone, H. E. Türeci, and S. Rotter, Phys. Rev. Lett. **108**, 173901 (2012).
[47] M. Brandstetter, M. Liertzer, C. Deutsch, P. Klang, J. Schöberl, H. E. Türeci, G. Strasser, K. Unterrainer, and S. Rotter, Nat. Commun. **5**, 4034 (2014).